HHS Public Access

Author manuscript

Health Phys. Author manuscript; available in PMC 2016 November 01.

Published in final edited form as:

Health Phys. 2015 November ; 109(5): 511–521. doi:10.1097/HP.0000000000000357.

DELAYED EFFECTS OF ACUTE RADIATION EXPOSURE IN A MURINE MODEL OF THE H-ARS: MULTIPLE-ORGAN INJURY CONSEQUENT TO <10 GY TOTAL BODY IRRADIATION

Joseph L. Unthank[*], **Steven J. Miller**[*], **Ariel K. Quickery**[*], **Ethan L. Ferguson**[†], **Meijing Wang**[*], **Carol H. Sampson**[†], **Hui Lin Chua**[†], **Matthew R. DiStasi**[‡], **Hailin Feng**[†], **Alexa Fisher**[†], **Barry P. Katz**[§], **P. Artur Plett**[†], **George E. Sandusky**[**], **Rajendran Sellamuthu**[†], **Sasidhar Vemula**[†], **Eric P. Cohen**[††], **Thomas J. MacVittie**[‡‡], and **Christie M. Orschell**[†]

[*]Department of Surgery, Indiana University School of Medicine, Indianapolis, IN

[†]Department of Medicine, Indiana University School of Medicine, Indianapolis, IN

[‡]Department of Pediatrics, Indiana University School of Medicine, Indianapolis, IN

[§]Department of Biostatistics, Indiana University School of Medicine, Indianapolis, IN

[**]Department of Pathology, Indiana University School of Medicine, Indianapolis, IN

[††]Radiation Oncology, Medical College of Wisconsin, Milwaukee, WI

[‡‡]Baltimore School of Medicine, University of Maryland, Baltimore, MD

Abstract

The threat of radiation exposure from warfare or radiation accidents raises the need for appropriate animal models to study the acute and chronic effects of high dose rate radiation exposure. The goal of this study was to assess the late development of fibrosis in multiple organs (kidney, heart, and lung) in survivors of the C57BL/6 mouse model of the hematopoietic-acute radiation syndrome (H-ARS). Separate groups of mice for histological and functional studies were exposed to a single uniform total body dose between 8.53 and 8.72 Gy of gamma radiation from a ^{137}Cs radiation source and studied 1–21 months later. Blood urea nitrogen levels were elevated significantly in the irradiated mice at 9 and 21 mo (from ~22 to 34 ± 3.8 and 69±6.0 mg/dl, $p<0.01$ vs non-irradiated controls) and correlated with glomerosclerosis (29±1.8% vs 64±9.7% of total glomeruli, $p<0.01$ vs non-irradiated controls). Glomerular tubularization and hypertrophy and tubular atrophy were also observed at 21 mo post-total body irradiation (TBI). An increase in interstitial, perivascular, pericardial and peri-bronchial fibrosis/collagen deposition was observed from ~9–21 mo post-TBI in kidney, heart and lung of irradiated mice relative to age-matched controls. Echocardiography suggested decreased ventricular volumes with a compensatory increase in left ventricular ejection fraction. The results indicate that significant delayed effects of acute radiation exposure occur in kidney, heart, and lung in survivors of the murine H-ARS TBI model which mirrors pathology detected in larger species and humans at higher radiation doses focused on specific organs.

For correspondence contact: Joseph L. Unthank, Ph.D., Department of Surgery, Indiana University School of Medicine, 975 West Walnut St., IB343, Indianapolis, IN 46202-5181, 317-274-7339 (voice), junthank@iupui.edu.

Keywords

Health effects; mice; radiation dose; radiation damage

INTRODUCTION

The threat of radiation exposure from warfare or radiation accidents raises the need for appropriate animal models to study the acute and chronic effects of high dose rate radiation exposure. Significant prompt radiation exposure may cause acute radiation syndromes (ARS) with gastrointestinal and or hematologic morbidity and mortality. Survivors of ARS will face the delayed effects of acute radiation exposure (DEARE), which includes a myriad of chronic illnesses affecting multiple organ systems. A better understanding of the mechanisms which mediate the long-term disease that develops in multiple organs is needed, as well as novel therapies to both improve the initial survival and mitigate DEARE. The challenges of studying DEARE are complicated by the absence of adequate experimental models and knowledge of radiation dose-response relationships as they pertain to latency, progression rates, and disease severity. The mouse is a useful model for studying the hematopoietic acute radiation syndrome (H-ARS) (Plett et al. 2012), as well as the acute (Booth et al. 2012) and chronic (Booth et al. 2012) gastrointestinal (GI) syndromes, and pulmonary DEARE (Jackson et al. 2012, Jackson et al. 2014). The authors have previously reported significant hematopoietic DEARE, termed residual bone marrow damage (RBMD), in survivors of a murine model of H-ARS after total body irradiation (TBI) with 7.76 Gy to 9.04 Gy (LD50/30 to LD90/30) (Chua et al. 2012, Chua et al. 2014). Models for pulmonary, renal, and cardiac DEARE have historically relied on partial body irradiation (PBI) where single high dose (>~10 Gy) radiation is directed at the organ of interest while shielding bone marrow and other organs to prevent early death from ARS. These studies have shown significant fibrosis, disrupting both normal tissue structure and function, in the kidney, heart and lung. Due to the reliance on PBI models for studying DEARE, there is little recent information available for DEARE in mice at radiation doses < 10 Gy in TBI models, such as those for H-ARS. The goal of this study was to assess DEARE in multiple organs (kidney, heart, and lung) in survivors of the C57BL/6 mouse model of H-ARS. We show that DEARE occurs in survivors of H-ARS, significantly affects kidney, heart, and lung, and mirrors pathology detected in larger species and humans at higher radiation doses.

MATERIALS AND METHODS

Mice and husbandry

All studies were approved by the Indiana University School of Medicine Institutional Animal Care and Use Committee. Specific pathogen free C57BL/6 mice (50/50 male/female; Jackson Laboratory, Bar Harbor, Maine) were received at 10 weeks of age and acclimated for 2 weeks prior to irradiation. Weights ranged from 15.0–22.5 g (females) and 20.0–28.0 g (males). Mice were identified by ear punch and/or tail marks. Husbandry and health status monitoring were carried out as previously described (Plett et al. 2012). Mice were housed in micro isolator cages and provided with autoclaved acidified water in sipper tubes on days 1–30 post-irradiation and wet feed between days 4–30 post-irradiation.

Irradiated mice were observed twice daily and scored on a scale of zero to three for signs meeting the criteria for early euthanasia based on the severity of hunched posture, squinted/closed eyes, and activity (Plett et al. 2012). Mice with total scores of eight or nine underwent euthanasia by cervical dislocation (Plett et al. 2012).

Survivors of the above acute radiation studies (n=5 studies) were used in the current studies of DEARE. These mice had been used as controls in studies where they were exposed, at 12 weeks of age, to the estimated LD50/30 to LD70/30 dose of radiation (range: 8.53 Gy to 8.72 Gy). At the end of those studies, surviving mice (IR mice) were transferred to the current studies, along with age-matched non-irradiated controls (NR mice). Separate groups of mice (n≥3 per group per assay) were used for histological studies of 1) kidney and heart or 2) lung; and functional studies with 3) echocardiography or 4) BUN at time points from 1–21 mo post-TBI.

Irradiation and dosimetry

Mice were placed in single chambers of a Plexiglas irradiation apparatus and were exposed to a single uniform total body dose between 8.53 and 8.72 Gy of gamma radiation from a ^{137}Cs radiation source (Mark 1 Irradiator, JL Shepherd, San Fernando, CA, ~1.00 Gy min^{-1}). To verify exposure, Landauer Inlight OSL nanodosimeters were placed in mouse phantoms and exposed along with the mice during every exposure. Nanodosimeters were read on a validated Landauer microStar reader calibrated with standard Dot dosimeters exposed with a NIST-traceable ^{137}Cs source (Battelle Memorial Institute, WA). Reproducibility of individual dots was 3±1% with accuracy of 4±2%, well within the 10% industry standard for experimental radiation dosimetry. Dose output checks (using farmer-type ion chambers and a validated electrometer), and dose field uniformity checks by exposing film, are performed annually by an onsite medical physicist.

Tissue harvest, fixation, histological staining, and imaging

All tissues were harvested following euthanasia by CO_2 inhalation. Kidney and heart were placed in RNA preservation solution followed by transfer to 10% neutral buffered formalin (NBF). Lungs were fixed overnight at room temperature in 10% NBF. Formalin-fixed tissues were paraffin embedded and sectioned, then stained with hematoxylin and eosin (H&E), Masson's trichrome, or picrosirius red.

For kidney and heart sections, digital images were acquired using a Leica DM 5000B microscope with a Diagnostic Instruments Spot RTKE camera and multiple sections from each mouse were evaluated for fibrosis and other specific pathological characteristics.

For lungs, the Aperio Scan Scope CS system was used (360 Park Center Drive Vista, CA 92081). All slides were imaged at 20×.

Assessment of radiation nephropathy

Histopathology is the gold standard for radiation nephropathy and blood urea nitrogen (BUN) is closely correlated with the degree of radiation-induced histopathological injury in

rodents (Cohen et al. 1996). Creatinine serum levels and clearance methods are problematic for mice and thus were not used (Bivona et al. 2011).

Blood Urea Nitrogen (BUN) Assay

BUN in serum was determined using a Pointe 180 Quick Touch analyzer with a BUN Reagent Set (Cat # B7552) and standard (20 mg/dl; Cat. # B7550-STD) from Pointe Scientific (Pointe Scientific Inc.; Canton, MI) according to supplied instructions. Blood was obtained either by cardiac puncture at the time of tissue harvest or by tail snip and processed to obtain serum. All samples were stored at −80 p°C prior to assay.

Renal histopathological analyses

A quantitative scoring system of radiation-induced renal histopathological changes previously developed by one of the coauthors for quantitative assessment of radiation nephropathy in rats (Moulder 1993, Sieber et al. 2011) was modified to assess radiation nephropathy in this model. The characteristics listed in Table 1 and described below were scored directly from images obtained at a magnification of 50–400×. Within each group, the individual scores were summed and averaged for the final score representing each group. Characteristics were determined as follows:

Sclerosed Glomeruli

H&E stained tissues were used to identify sclerosed glomeruli. A glomerulus was identified as sclerosed if 50% or more of the cellular material lacked evenly dispersed nuclei or capillaries, and showed an increase in collagen deposition (see Supplemental Data Figure 1). At least 20 random glomeruli per mouse were marked as normal or sclerosed using Image J. The percentage of sclerosed glomeruli for each mouse was calculated, and a numerical scale was developed from the percentage data (Table 1).

Hypertrophied glomeruli

A glomerulus was considered hypertrophied if its diameter was ≥ 120um (Table 1), based upon results of the histogram for glomerular diameters of the various groups.

Tubularized glomeruli

Each kidney section was assessed for tubularization by parietal epithelium evidenced as cuboidal epithelial cells lining Bowmen’s capsule (Table 1, Supplemental Figure 3).

Interstitial Fibrosis

A numerical scale was developed based on qualitative descriptors of images from 50× to 200× (Table 1, Supplemental Data Figure 4).

Protein Casts

A scale was developed from the quantitative data for total counts per slide (Table 1, Supplemental Data Figure 5).

In addition, the area and diameter of Bowman's capsules were determined by morphometric analyses using Image J. Representative images were obtained from picrosirius red-stained tissue sections at 50×, the images were digitally enlarged to 150%, and the cross-sectional areas of ≥20 random Bowman's capsules per animal were traced and average diameter calculated from the circumference, assuming circular shape.

Analysis of cardiac function, fibrosis, and Nox2 expression

Myocardial Function and Dimensions—The left ventricular (LV) images of echocardiography were obtained using parasternal short-axis two-dimensional M-mode echocardiograms (VisualSonics Vevo-2100) at the level of the papillary muscle in animals at 18 months post-TBI. LV function (ejection fraction – EF, and fractional shortening – FS), LV mass and volume were calculated by using measurements of diastolic and systolic inner ventricular septum over more than three cardiac cycles.

Pericardial, interstitial and peri-vascular fibrosis—Interstitial fibrosis was assessed as described in Table 1. The average thickness of the pericardial collagen was calculated with ImageJ by thresholding the area with picrosirius red staining in a region of interest (ROI) containing only the pericardium and then dividing by length of the pericardium in the ROI (~500um).

Expression of left ventricular Nox2 mRNA—Relative differences between TBI and non-irradiated mouse heart Nox2 subunit mRNA expression were determined using reverse transcription real-time quantitative PCR (RT-qPCR) as previously described in detail (Miller et al. 2010, Distasi et al. 2014). Heart tissue stored in RNA preservation solution was used for purification of total RNA and aliquots (1.0 μg) were reverse transcribed into cDNA. For PCR, cDNA (5.0 μl, 1:50 dilution) was combined with primers and probes for Nox2 or EIF2B1 endogenous control (TaqMan Gene Expression Assays; Applied Biosystems, Foster City, CA) in the presence of a PCR master mix (FastStart Universal Probe Master Mix; Roche Applied Science, Indianapolis, IN). Reactions were run in triplicate on an Applied Biosystems 7500 Real-Time PCR System using relative quantification (ddCt) with standard two-step 7500 PCR cycling conditions (40 cycles). Differences in PCR product yields between groups were determined by comparing the fold differences between target mRNA after normalization to EIF2B1.

Pulmonary fibrosis—Computer-assisted morphometric analysis of digital images was done using the included software of the Aperio Imaging system. The positive pixel algorithm was modified to quantify the blue collagen staining of Masson's Trichrome in lungs of irradiated mice and non-irradiated, age-matched controls. Histological scoring was also done utilizing an established scale with eight grades of pulmonary fibrosis (Ashcroft et al. 1988).

RESULTS

Renal function and pathology

As shown in Figure 1, BUN levels in IR mice were similar to NI at 4 mo post-TBI but were increased significantly by 9 mo and were further elevated by 21 mo post-TBI. Examination of kidney cross-sections of irradiated mice at 9 and 21 mo post-TBI and age-matched controls demonstrated significant abnormalities as summarized in Table 2. The most apparent abnormalities present at 9 mo post-TBI were glomerulosclerosis and diffuse interstitial collagen deposition (Table 2 and Figure 2, Supplemental Figure 1). Glomerulosclerosis was observed in 29±1.8% of the glomeruli of the irradiated mice at 9 mo post-TBI vs. 0.4±0.4% on the non-irradiated, age-matched controls. At 21 mo post-TBI, the glomerular pathology had advanced as evidenced by increased glomerulosclerosis (64±9.7% vs. 1.6±0.5% in non-irradiated, age-matched controls. Glomerular tubularization and hypertrophy were also observed in kidneys of irradiated mice at 21 mo post-TBI (Table 2, Figure 2, Supplemental Figures 2 and 3). Glomerular areas were measured and averaged diameters calculated and presented as histograms in Figure 3 with descriptive statistics in Table 3 to demonstrate the glomerular hypertrophy that occurred in the irradiated mice at 21 mo post-TBI. Note the maximum diameter of 120 um in the non-irradiated 1 yr old mice; diameters greater than this were considered to indicate hypertrophied glomeruli. In the renal cross-sections from the irradiated mice, increased collagen deposition was apparent in trichrome and picrosirius red stained sections (Table 2, Figure 2 and Supplemental Figure 4). Tubular atrophy was apparent from focal areas of interstitial fibrosis and glomerular crowding (Figure 2D). Renal casts were also significantly increased in number in the irradiated mice at 21 mo (Table 2, Supplemental Figure 5).

Cardiovascular pathology

Representative micrographs of picrosirius red staining of heart sections are shown in Figure 4. Diffuse interstitial fibrosis/increased collagen deposition was observed at 9 m post-TBI relative to age-matched NI. In 2 yr old mice, diffuse interstitial fibrosis was observed in both NI and IR, but was greater in the IR. In addition, significant focal fibrosis with loss of myocytes was observed in 2 of the 4 IR mice at 21 mo post-TBI (Figure 4E and F). Notable changes in coronary arteries were apparent only at 21 mo post-TBI where the vessels showed increased perivascular collagen and loss of vascular smooth muscle cells as illustrated in Figure 4D and E. Pericardial collagen was also increased in the irradiated mice as seen in the micrographs of Figure 4A–D and quantified in Figure 5. Assessment of left ventricular Nox2 mRNA expression by qPCR demonstrated a significant elevation in IR relative to NI at both 9 and 21 mo post-TBI as shown in Figure 6. Results of echocardiography indicated a decrease in ventricular volumes and suggested a compensatory increase in left ventricular ejection fraction (Figure 7).

Pulmonary Fibrosis

Gross inspection of lung samples stained with Masson’s trichrome showed an initial increase of peribronchial and perivascular collagen deposition at 6–7 mo post-TBI when compared to 1.5 mo IR mice, followed by increased interstitial collagen deposition and more prominent perivascular deposition at 19 mo (Figure 8). Lung sections analyzed using whole

slide digital analysis demonstrated significantly increased pulmonary fibrosis in H-ARS survivors by 19 months post-TBI compared to earlier time points (Figure 9A). Analysis using a manual pathology hand count (Ashcroft et al. 1988) showed significantly increased fibrosis at 19 months post-TBI compared to each of the earlier time points for both NI and IR groups ($p<0.0001$), and significantly increased fibrosis in IR mice compared to NI mice at 19 months post-TBI (Figure 9B).

DISCUSSION

The results of our study demonstrate significant DEARE in C57BL/6 mice exposed to total body irradiation at approximately the LD50/30 – LD70/30 dose for H-ARS (8.5 – 8.7 Gy). Fibrosis is manifested in kidney, heart, and lung by 6–9 months post-TBI with substantial progression by 18–21 mo. In the sections below, the observations in each of these organs are discussed in terms of previous studies and potential significance.

Renal function and pathology

BUN is an excellent noninvasive surrogate marker of radiation-induced renal dysfunction and histopathological injury (Cohen et al. 1996, Williams et al. 2010). Our results indicate elevation of BUN by 9 mo post-TBI in mice that survived H-ARS after a single TBI dose of 853–904 cGy (actual LD60–90/30) and even higher BUN at 21 mo post-TBI in mice that received 872–904 cGy (actual LD 41–65/30). These results are consistent with the report by Down et al. (Down et al. 1990) in which BUN elevation was observed to occur after 6 mo in C3H mice that received fractionated TBI at total doses between 11–15 Gy followed by syngeneic bone marrow transplantation.

Our current results show the early manifestation of radiation nephropathy in this model to be primarily glomerular pathology with interstitial fibrosis and tubular atrophy occurring later. This is consistent with early mouse studies in other strains. In 1954 Furth et al. (Furth et al. 1954) reported on late effects in LAF_1 mice of ionizing radiation from an experimental nuclear detonation. The predominant source of radiation was high energy gamma rays. Nephrosclerosis was one of the major non-neoplastic disorders and was observed at doses greater than 500r. The renal pathology observed at 30 mo after exposure included glomerular obliteration, arteriolar sclerosis, and diffuse interstitial fibrosis. A follow-up report in 1960 (Upton et al. 1960) noted that nephrosclerosis increased with radiation dose in frequency, severity and rate of progression for kidneys collected during necropsy. The earliest morphological abnormalities in kidneys were noted in glomerular capillaries which exhibited basement membrane thickening. With severe disease, fibrinoid necrosis of glomerular capillaries, juxtaglomerular arterioles, and larger arterioles was observed. Complete glomerular scarring and marked tubular dilatation and atrophy was noted in the most advanced cases. Cosgrove et al. (Cosgrove et al. 1965) performed a study in the same LAF_1 mice but with X-ray irradiation at 10 wks or 12 mo of age. Significant renal pathology was noted at the time of death in mice which had survived the initial 30 days post-irradiation period. They also reported that injury was primarily glomerular and considered tubular atrophy to be secondary to the glomerular changes. Glomerulosclerosis was reported to be grossly evident about 9 months post-exposure and occurred at doses ≥ LD50/30. At similar

time points post-TBI, the frequency and severity of disease was greater in the older mice. This progression is also consistent the development of renal pathology after local X-irradiation of mouse kidneys reported by Glatstein et al. (Glatstein et al. 1977) and whole mouse exposure to fractionated gamma irradiation by Down et al. (Down et al. 1990). Both of these groups reviewed studies indicating the glomerular changes in the mouse to be similar to those that occur in human radiation nephropathy.

Our data show that radiation nephropathy is a definite component of DEARE occurring after survivable radiation exposures. Further, recent long-term studies of Hiroshima-Nagasaki survivors show that there is increased chronic kidney disease many years after single fraction exposures in the 100 to 200 cGy range (Adams et al. 2012, Sera et al. 2013). Kidneys are thus not radio-resistant and renal radiation injury is a substantial risk after accidental or belligerent exposures.

Cardiovascular pathology

To our knowledge, previous studies of the effects of whole body irradiation on mouse cardiac function and pathology are not available. In response to local irradiation of the mouse heart, Seeman et al. (Seemann et al. 2012) reported progressive myocardial and vascular damage but only modest changes in cardiac function. After total body irradiation (10 Gy) in a rat model, Baker et al. (Baker et al. 2009) reported impaired cardiac function that was associated with vascular degeneration and fibrosis. Yarom et al. (Yarom et al. 1993) reported epicardial and endocardial fibrosis of left and right ventricle of rats at 3 and 6 mo after local cardiac irradiation (20 Gy). This fibrosis was associated with decreased heart rate and cardiac output at 6 mo post-irradiation. The limited number of available studies is likely the result of the heart being considered to be relatively insensitive to ionizing radiation (Leach and Sugiura 1941, Robert Stewart and Fajardo 1984) until recently (Little et al. 2012) (Shimizu et al. 2010) (Ivanov et al. 2006). Our observations of pericardial, myocardial, and perivascular fibrosis are consistent with these previous reports in animals and also of clinical studies (Little et al. 2012) (Shimizu et al. 2010) (Robert Stewart and Fajardo 1984, Veinot and Edwards 1996, Virmani et al. 1999, Ivanov et al. 2006). The role of renal dysfunction on cardiovascular pathology (Adams et al. 2012, Lenarczyk et al. 2013, Sera et al. 2013) and of microvascular injury (Fajardo and Stewart 1971, Yarom et al. 1993, Baker et al. 2009, Seemann et al. 2012) and Nox2 (Johar et al. 2006, Bache and Chen 2014, Murdoch et al. 2014) in the fibrotic response subsequent to whole body irradiation are among the questions that require more investigation.

Pulmonary Fibrosis

Most earlier experimental studies of radiation-induced lung injury have used models with much higher doses of radiation (11 to 16 Gy) directed at the thoracic cavity to avoid most of the marrow and gastrointestinal (GI) tract and accompanying lethal H-ARS and GI-ARS (Jackson et al. 2012, Jackson et al. 2014). In contrast, H-ARS radiation doses used in the current study were much lower (8.53 to 8.72 Gy), but were total body in nature, which likely has the result of increased latency compared to whole-thoracic irradiation (WTI) models. Lung injury occurring from total body irradiation may manifest differently than that in WTI models due to secondary effects imparted from radiation damaged tissues not normally

exposed in WTI models. Lung injury in the C57BL/6 strain after WTI manifests as pleural effusions rather than pneumonitis and, as such, it has been suggested that C57BL/6 mice may not be the best model for human disease (Jackson et al. 2012, Jackson et al. 2014). In addition, the LD50/180 is much higher for C57BL/6 mice (14.17 Gy) than for C57L mice (11.35 Gy), which have an LD50/180 closer to that for non-human primates and humans (Van Dyk et al. 1981, Garofalo et al. 2014, Jackson et al. 2014) and as such, have been proposed as a more appropriate radiation lung injury model for humans (Jackson et al. 2012, Jackson et al. 2014).

CONCLUSION

The specific pathologies observed in the current report within the kidneys and heart are similar to those in clinical reports. The observations of significant pathology at these relatively low radiation doses, compared to those used in partial body exposure models that focus high dose exposures on specific organs while sparing of bone marrow and GI, may reflect multi-organ interactions, such as have been reported between kidney and heart (Lenarczyk et al. 2013). The C57BL/6 mouse H-ARS model thus appears to be an appropriate model for some aspects of DEARE, and potentially valuable for the assessment of mitigators on H-ARS survival as well as DEARE. The widespread availability of genetic modifications in this species and strain also make it well suited to elucidate mechanisms of the radiation-induced injury in these organs.

Supplementary Material

Refer to Web version on PubMed Central for supplementary material.

Acknowledgments

Support: This project has been funded in whole or in part with Federal funds from the National Institute of Allergy and Infectious Diseases, National Institutes of Health, Department of Health and Human Services, under Contract No. HHSN272201000046C, HHSN266200500043C, and 1U01AI107340-01 and with resources and the use of facilities at the Clement J Zablocki Medical Center in Milwaukee, WI.

LITERATURE CITED

Adams MJ, Grant EJ, Kodama K, Shimizu Y, Kasagi F, Suyama A, Sakata R, Akahoshi M. Radiation dose associated with renal failure mortality: A potential pathway to partially explain increased cardiovascular disease mortality observed after whole-body irradiation. Radiat Res. 2012; 177:220–228. [PubMed: 22149958]

Ashcroft T, Simpson JM, Timbrell V. Simple method of estimating severity of pulmonary fibrosis on a numerical scale. J Clin Pathol. 1988; 41:467–470. [PubMed: 3366935]

Bache RJ, Chen Y. Nox2-induced myocardial fibrosis and diastolic dysfunction role of the endothelium. J Am Coll Cardiol. 2014; 63:2742–2744. [PubMed: 24681139]

Baker JE, Fish BL, Su J, Haworth ST, Strande JL, Komorowski RA, Migrino RQ, Doppalapudi A, Harmann L, Allen Li X, Hopewell JW, Moulder JE. 10 gy total body irradiation increases risk of coronary sclerosis, degeneration of heart structure and function in a rat model. Int J Radiat Biol. 2009; 85:1089–1100. [PubMed: 19995235]

Bivona BJ, Park S, Harrison-Bernard LM. Glomerular filtration rate determinations in conscious type ii diabetic mice. American Journal of Physiology - Renal Physiology. 2011; 300:F618–F625. [PubMed: 21147841]

Booth C, Tudor G, Tonge N, Shea-Donohue T, MacVittie TJ. Evidence of delayed gastrointestinal syndrome in high-dose irradiated mice. Health Phys. 2012; 103:400–410. [PubMed: 23091877]

Booth C, Tudor G, Tudor J, Katz BP, MacVittie TJ. Acute gastrointestinal syndrome in high-dose irradiated mice. Health Phys. 2012; 103:383–399. [PubMed: 23091876]

Chiu Y-T, Liu S-k, Liu M, Chen SP, Lin YH, Mao SJT, Chu R. Characterization and quantitation of extracellular collagen matrix in myocardium of pigs with spontaneously occurring hypertrophic cardiomyopathy. Cardiovascular Pathology. 1999; 8:169–175. [PubMed: 10722240]

Chua HL, Plett PA, Sampson CH, Joshi M, Tabbey R, Katz BP, MacVittie TJ, Orschell CM. Long-term hematopoietic stem cell damage in a murine model of the hematopoietic syndrome of the acute radiation syndrome. Health Phys. 2012; 103:356–366. [PubMed: 22929468]

Chua HL, Plett PA, Sampson CH, Katz BP, Carnathan GW, MacVittie TJ, Lenden K, Orschell CM. Survival efficacy of the pegylated g-csfs maxy-g34 and neulasta in a mouse model of lethal h-ars, and residual bone marrow damage in treated survivors. Health Phys. 2014; 106:21–38. [PubMed: 24276547]

Cohen EP, Molteni A, Hill P, Fish BL, Ward WF, Moulder JE, Carone FA. Captopril preserves function and ultrastructure in experimental radiation nephropathy. Lab Invest. 1996; 75:349–360. [PubMed: 8804358]

Cosgrove GE, Upton AC, Smith LH, Dent JN. Radiation glomerulosclerosis and other late effects: Influence of radiological factors and aet. Radiat Res. 1965; 25:725–735. [PubMed: 14330503]

Distasi MR, Unthank JL, Miller SJ. Nox2 and p47phox modulate compensatory growth of primary collateral arteries. Am J Physiol Heart Circ Physiol. 2014; 306:H1435–H1443. [PubMed: 24633549]

Down JD, Berman AJ, Warhol M, Yeap B, Mauch P. Late complications following total-body irradiation and bone marrow rescue in mice: Predominance of glomerular nephropathy and hemolytic anemia. Int J Radiat Biol. 1990; 57:551–565. [PubMed: 1968948]

Fajardo LF, Stewart JR. Capillary injury preceding radiation-induced myocardial fibrosis. Radiology. 1971; 101:429–433. [PubMed: 5114783]

Furth J, Upton AC, Christenberry KW, Benedict WH, Moshman J. Some late effects in mice of ionizing radiation from an experimental nuclear detonation. Radiology. 1954; 63:562–570. [PubMed: 13204618]

Garofalo M, Bennett A, Farese AM, Harper J, Ward A, Taylor-Howell C, Cui W, Gibbs A, Lasio G, Jackson W 3rd, MacVittie TJ. The delayed pulmonary syndrome following acute high-dose irradiation: A rhesus macaque model. Health Phys. 2014; 106:56–72. [PubMed: 24276550]

Glatstein E, Fajardo LF, Brown JM. Radiation injury in the mouse kidney—i sequential light microscopic study. International Journal of Radiation Oncology*Biology*Physics. 1977; 2:933–943.

Ivanov VK, Maksioutov MA, Chekin SY, Petrov AV, Biryukov AP, Kruglova ZG, Matyash VA, Tsyb AF, Manton KG, Kravchenko JS. The risk of radiation-induced cerebrovascular disease in chernobyl emergency workers. Health Phys. 2006; 90:199–207. [PubMed: 16505616]

Jackson IL, Xu P, Hadley C, Katz BP, McGurk R, Down JD, Vujaskovic Z. A preclinical rodent model of radiation-induced lung injury for medical countermeasure screening in accordance with the fda animal rule. Health Phys. 2012; 103:463–473. [PubMed: 22929472]

Jackson IL, Xu P, Hadley C, Katz BP, McGurk R, Down JD, Vujaskovic Z. A preclinical rodent model of radiation-induced lung injury for medical countermeasure screening in accordance with the fda animal rule. Health Physics. 2012; 103:463–473. 10.1097/HP.0b013e31826386ef. [PubMed: 22929472]

Jackson IL, Xu PT, Nguyen G, Down JD, Johnson CS, Katz BP, Hadley CC, Vujaskovic Z. Characterization of the dose response relationship for lung injury following acute radiation exposure in three well-established murine strains: Developing an interspecies bridge to link animal models with human lung. Health Phys. 2014; 106:48–55. [PubMed: 24276549]

Jackson IL, Xu PT, Nguyen G, Down JD, Johnson CS, Katz BP, Hadley CC, Vujaskovic Z. Characterization of the dose response relationship for lung injury following acute radiation exposure in three well-established murine strains: Developing an interspecies bridge to link animal models with human lung. Health Phys. 2014; 106:48–55. [PubMed: 24276549]

Johar S, Cave AC, Narayanapanicker A, Grieve DJ, Shah AM. Aldosterone mediates angiotensin ii-induced interstitial cardiac fibrosis via a nox2-containing nadph oxidase. The FASEB Journal. 2006; 20:1546–1548. [PubMed: 16720735]

Leach JE, Sugiura K. The effect of high voltage roentgen rays on the heart of adult rats. Am J Roentgenol. 1941; 45:414–425.

Lenarczyk M, Lam V, Jensen E, Fish BL, Su J, Koprowski S, Komorowski RA, Harmann L, Migrino RQ, Li XA, Hopewell JW, Moulder JE, Baker JE. Cardiac injury after 10 gy total body irradiation: Indirect role of effects on abdominal organs. Radiat Res. 2013; 180:247–258. [PubMed: 23919311]

Little MP, Azizova TV, Bazyka D, Bouffler SD, Cardis E, Chekin S, Chumak VV, Cucinotta FA, de Vathaire F, Hall P, Harrison JD, Hildebrandt G, Ivanov V, Kashcheev VV, Klymenko SV, Kreuzer M, Laurent O, Ozasa K, Schneider T, Tapio S, Taylor AM, Tzoulaki I, Vandoolaeghe WL, Wakeford R, Zablotska LB, Zhang W, Lipshultz SE. Systematic review and meta-analysis of circulatory disease from exposure to low-level ionizing radiation and estimates of potential population mortality risks. Environ Health Perspect. 2012; 120:1503–1511. [PubMed: 22728254]

Miller SJ, Coppinger BJ, Zhou X, Unthank JL. Antioxidants reverse age-related collateral growth impairment. J Vasc Res. 2010; 47:108–114. [PubMed: 19729957]

Moulder JE, Fish BL, Cohen EP. Noncontinuous use of angiotensin converting enzyme inhibitors in the treatment of experimental bone marrow transplant nephropathy. Bone Marrow Transplant. 1997; 19:729–735. [PubMed: 9156251]

Murdoch CE, Chaubey S, Zeng L, Yu B, Ivetic A, Walker SJ, Vanhoutte D, Heymans S, Grieve DJ, Cave AC, Brewer AC, Zhang M, Shah AM. Endothelial nadph oxidase-2 promotes interstitial cardiac fibrosis and diastolic dysfunction through proinflammatory effects and endothelial-mesenchymal transition. J Am Coll Cardiol. 2014; 63:2734–2741. [PubMed: 24681145]

Plett PA, Sampson CH, Chua HL, Joshi M, Booth C, Gough A, Johnson CS, Katz BP, Farese AM, Parker J, MacVittie TJ, Orschell CM. Establishing a murine model of the hematopoietic syndrome of the acute radiation syndrome. Health Phys. 2012; 103:343–355. [PubMed: 22929467]

Plett PA, Sampson CH, Chua HL, Joshi M, Booth C, Gough A, Johnson CS, Katz BP, Farese AM, Parker J, MacVittie TJ, Orschell CM. Establishing a murine model of the hematopoietic syndrome of the acute radiation syndrome. Health Phys. 2012; 103:343–355. [PubMed: 22929467]

Robert Stewart J, Fajardo LF. Radiation-induced heart disease: An update. Prog Cardiovasc Dis. 1984; 27:173–194. [PubMed: 6387801]

Seemann I, Gabriels K, Visser NL, Hoving S, te Poele JA, Pol JF, Gijbels MJ, Janssen BJ, van Leeuwen FW, Daemen MJ, Heeneman S, Stewart FA. Irradiation induced modest changes in murine cardiac function despite progressive structural damage to the myocardium and microvasculature. Radiother Oncol. 2012; 103:143–150. [PubMed: 22112779]

Sera N, Hida A, Imaizumi M, Nakashima E, Akahoshi M. The association between chronic kidney disease and cardiovascular disease risk factors in atomic bomb survivors. Radiat Res. 2013; 179:46–52. [PubMed: 23148507]

Shimizu Y, Kodama K, Nishi N, Kasagi F, Suyama A, Soda M, Grant EJ, Sugiyama H, Sakata R, Moriwaki H, Hayashi M, Konda M, Shore RE. Radiation exposure and circulatory disease risk: Hiroshima and nagasaki atomic bomb survivor data, 1950–2003. BMJ. 2010; 340

Sieber F, Muir SA, Cohen EP, Fish BL, Mäder M, Schock AM, Althouse BJ, Moulder JE. Dietary selenium for the mitigation of radiation injury: Effects of selenium dose escalation and timing of supplementation. Radiat Res. 2011; 176:366–374. [PubMed: 21867430]

Upton AC, Kimball AW, Furth J, Christenberry KW, Benedict WH. Some delayed effects of atom-bomb radiations in mice. Cancer Res. 1960; 20:1–60. [PubMed: 13779232]

Van Dyk J, Keane TJ, Kan S, Rider WD, Fryer CJH. Radiation pneumonitis following large single dose irradiation: A re-evaluation based on absolute dose to lung. International Journal of Radiation Oncology*Biology*Physics. 1981; 7:461–467.

Veinot JP, Edwards WD. Pathology of radiation-induced heart disease: A surgical and autopsy study of 27 cases. Hum Pathol. 1996; 27:766–773. [PubMed: 8760008]

Virmani R, Farb A, Carter AJ, Jones RM. Pathology of radiation-induced coronary artery disease in human and pig. Cardiovasc Radiat Med. 1999; 1:98–101. [PubMed: 11272363]

Williams JP, Brown SL, Georges GE, Hauer-Jensen M, Hill RP, Huser AK, Kirsch DG, MacVittie TJ, Mason KA, Medhora MM, Moulder JE, Okunieff P, Otterson MF, Robbins ME, Smathers JB, McBride WH. Animal models for medical countermeasures to radiation exposure. Radiat Res. 2010; 173:557–578. [PubMed: 20334528]

Yarom R, Harper IS, Wynchank S, Schalkwyk Dv, Madhoo J, Williams K, Salie R, Genade S, Lochner A. Effect of captopril on changes in rats' hearts induced by long-term irradiation. Radiat Res. 1993; 133:187–197. [PubMed: 8438060]

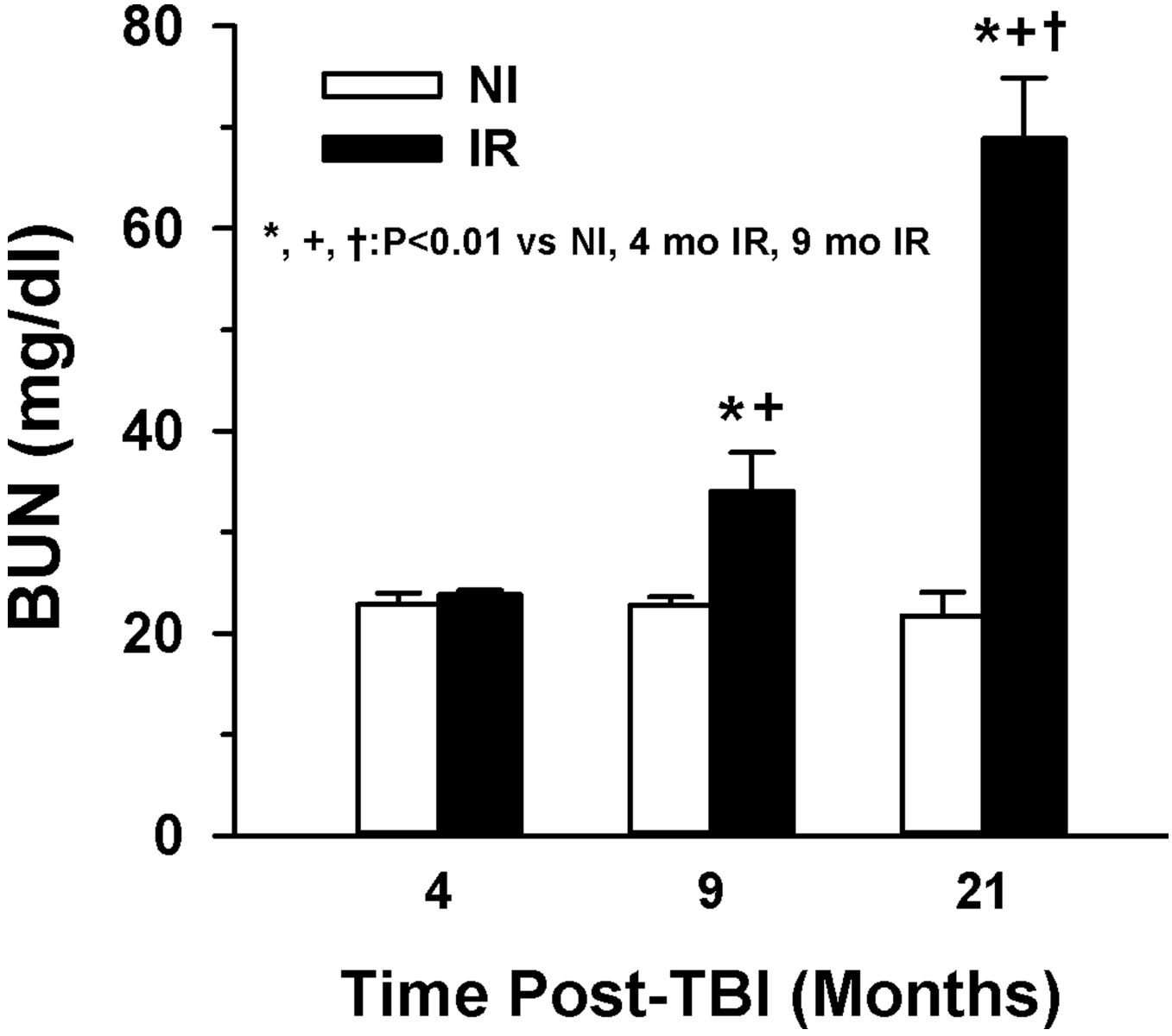

Fig. 1.

Blood Urea Nitrogen (BUN) increased with time post-TBI in irradiated mice. BUN was determined in serum obtained from non-irradiated (NI) and irradiated (IR; 853–904 cGy; LD41–90/30) age-matched mice at three time points post-TBI. BUN was significantly elevated in IR mice at 9 (n=7) and 21 (n=5 NI, 4 IR) mo post-TBI compared to 4 (n=11 NI, 16 IR) mo post-TBI. Evaluation of potential effects on BUN due to blood collection methods, gender, or radiation dose indicated no statistical difference in the values obtained at any time post-TBI. Error bars are standard error of mean.

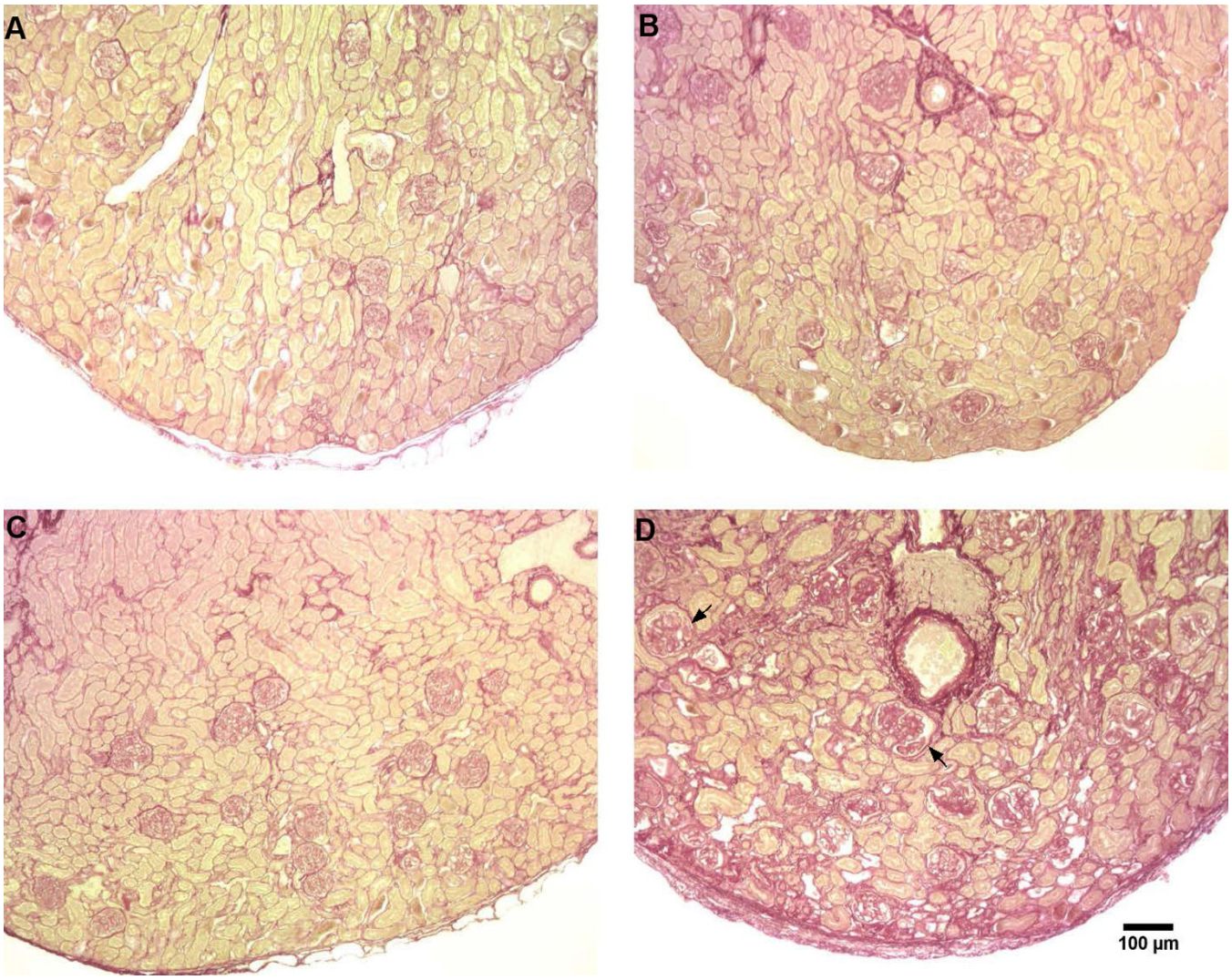

Fig. 2.

Representative micrographs of renal cross-sections stained with Picrosirius red. Increased red staining for collagen in seen in the glomeruli of the IR at 9 mo post-TBI (B) relatively to the age-matched NI control. At 21 mo post-TBI, the IR mice (D) but not the age-matched NI controls (C) had significant interstitial fibrosis with tubular atrophy, increased glomerular collagen, and hypertrophied glomeruli (arrows).

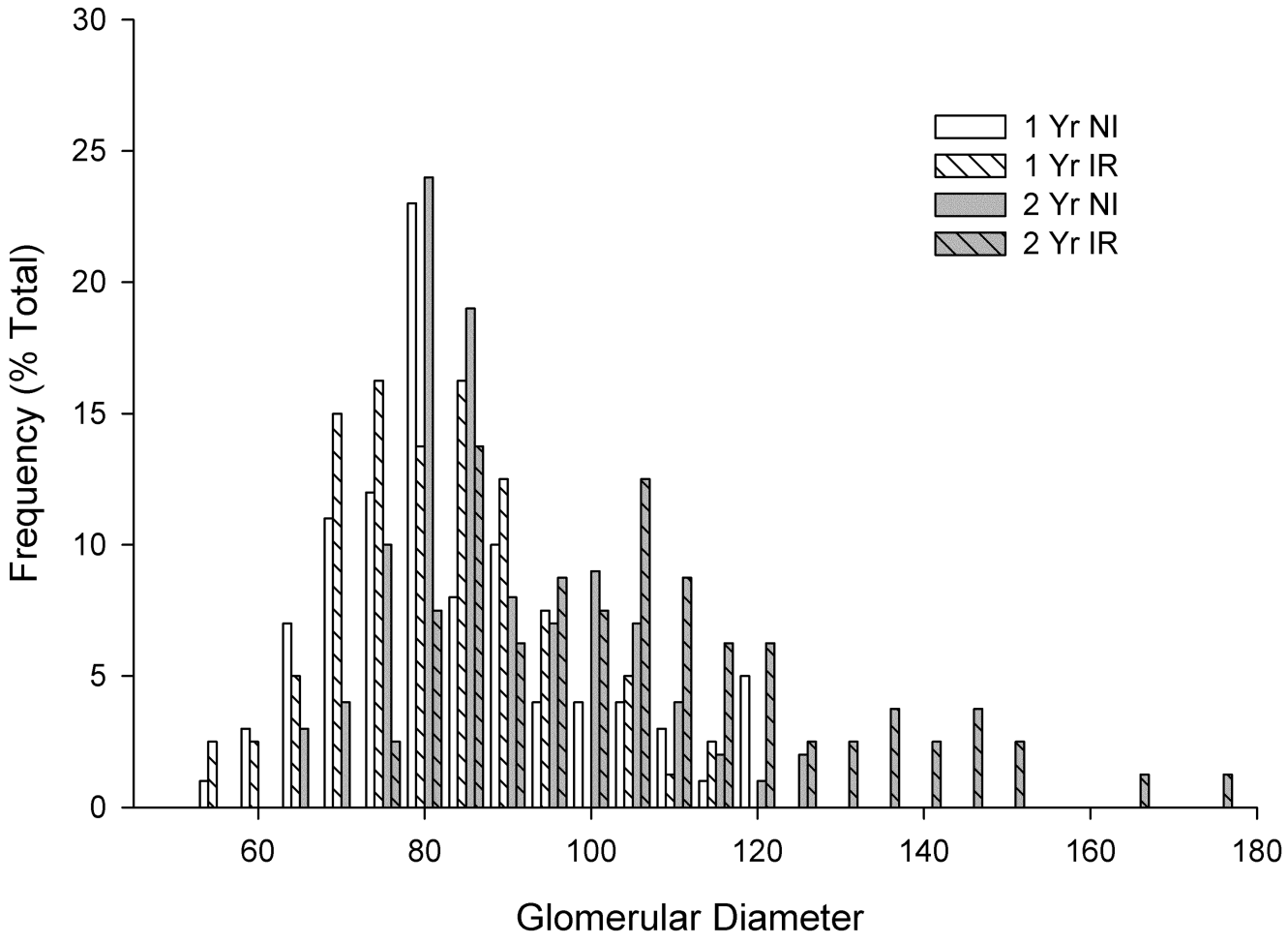

Fig. 3.

Histograms of glomerular diameters at NI and IR mice at 9 and 21 mo post-TBI. The area inside Boman's capsules seen in micrographs was traced with ImageJ and diameter calculated from the circumference. The histogram for the 21 mo post-TBI IR mice is shifted to the right with increased diameters. Descriptive statistics are presented in Table 3.

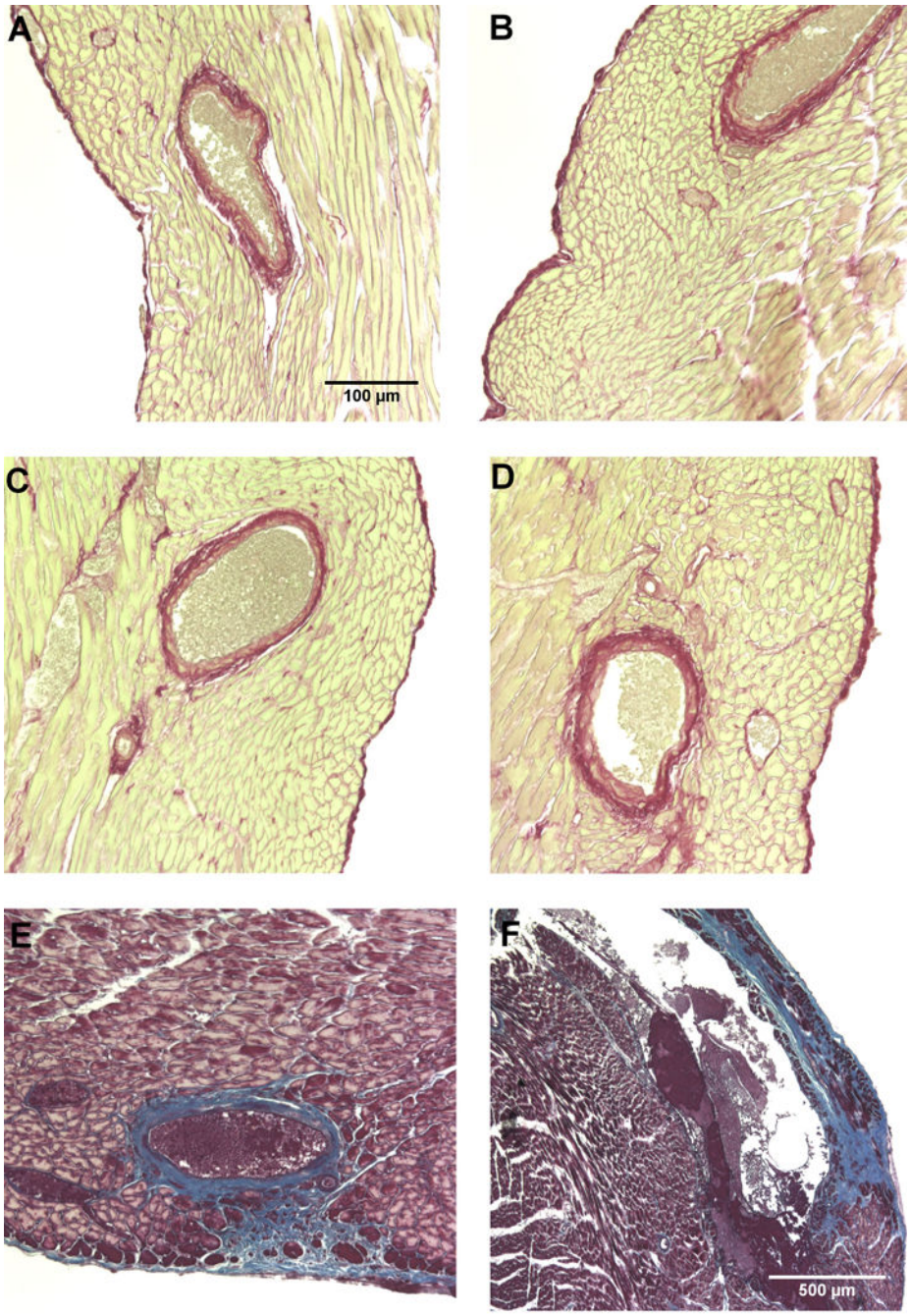

Fig. 4.

Representative micrographs of heart cross-sections from NI and IR mice stained with Picrosirius red (A–D) or Masson's trichrome (E, F). A and C represent the left ventricle of NI mice and B and D IR mice at 9 and 21 mo post-TBI, respectively. The thickness of the collagen stain is increased in the pericardium in the IR mice represented by B and D relative to age-matched controls. Peri-arterial staining was also increased in the IR mice, especially at 21 mo post-TBI and focal regions of interstitial fibrosis were consistently observed in the IR mice. A characteristic noted only in the IR mice at 21 mo post-TBI was limited staining

for vascular smooth muscle but increased collagen staining in the media of the coronary arteries as shown in E. The images in A–E were obtained at the same magnification which is indicated by the scale bar in A. Half of the IR mice at 21 mo post-TBI had regions of significant fibrosis with loss of myocytes which occurred in both the left (E) and right (F) ventricle.

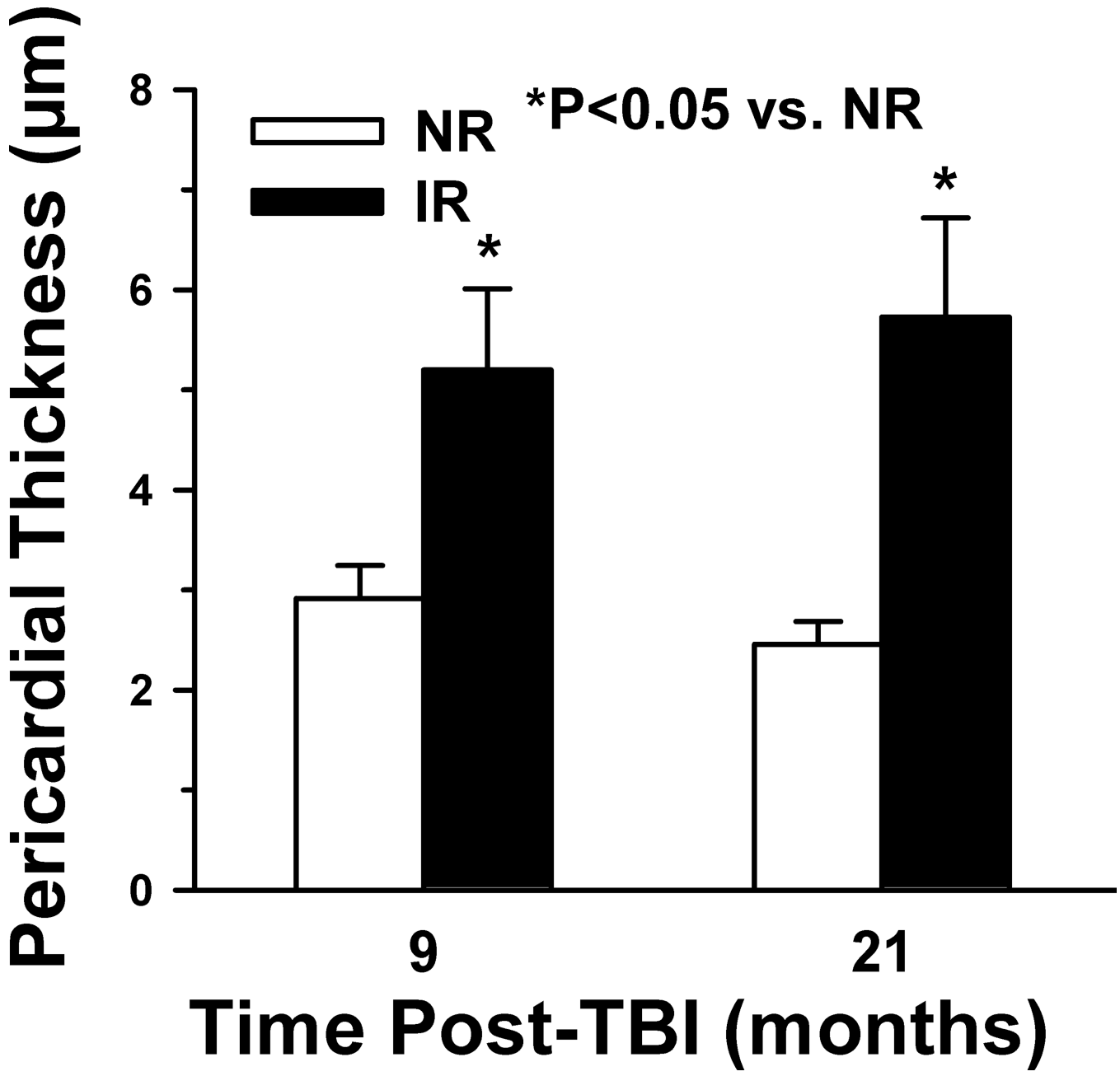

Fig. 5.

Pericardial collagen thickness significantly increased time post-TBI in irradiated (IR) vs. non-irradiated (NI) heart. The plot shows the calculated average thickness of the pericardial collagen. N=3–4. Error bars are standard error of mean.

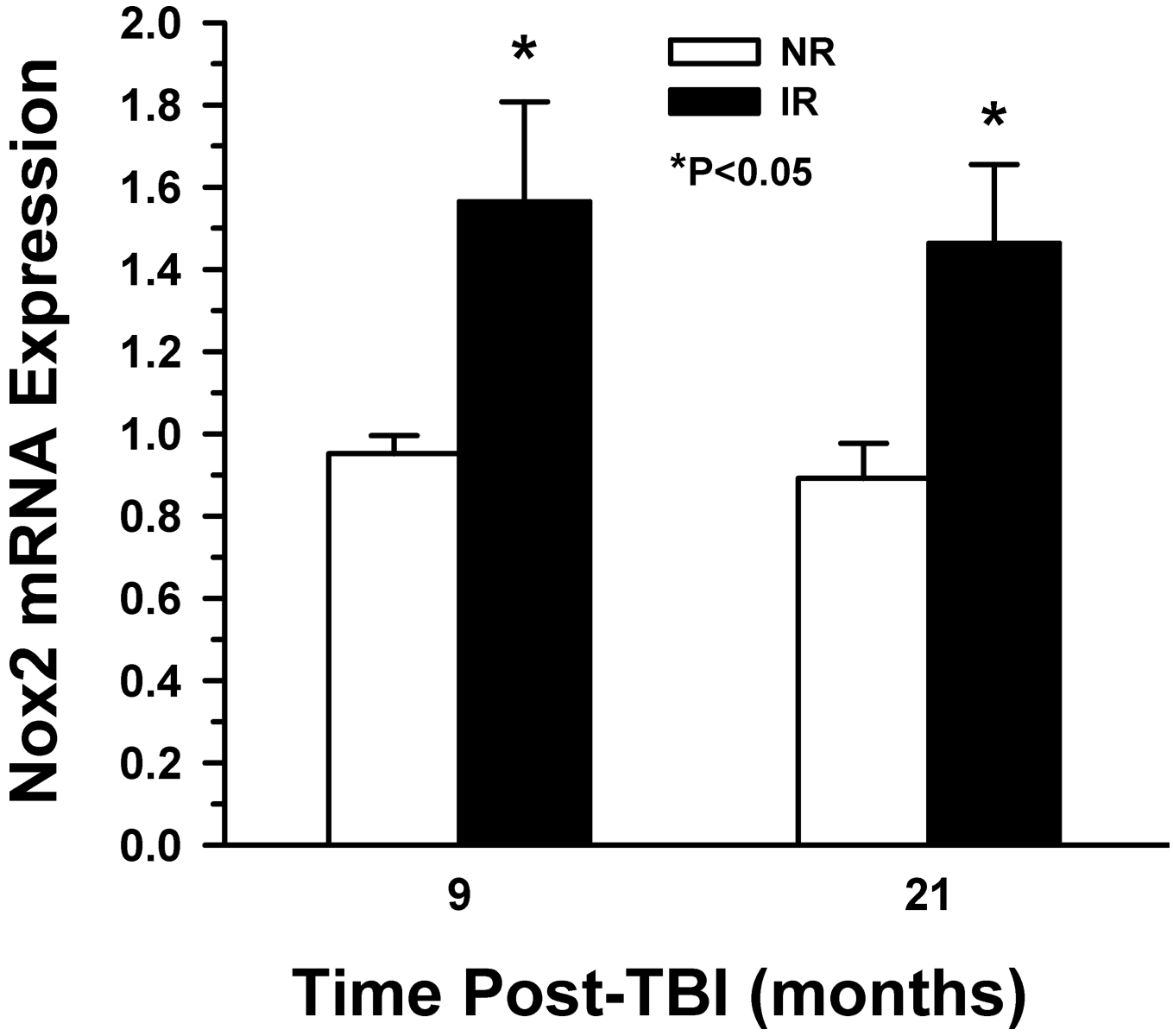

Fig. 6.

Nox2 expression increased with time post-TBI in irradiated mice. Relative changes in Nox2 mRNA expression were assessed by qPCR. Compared to the non-irradiated age-matched controls (NI), irradiated (IR) mice at 9 mo (n=4) post-TBI had significantly increased Nox2 expression in the left ventricle (n=4) and a trend at 21 mo (n=5 NI, 2 IR) post-TBI. Error bars are standard error of mean.

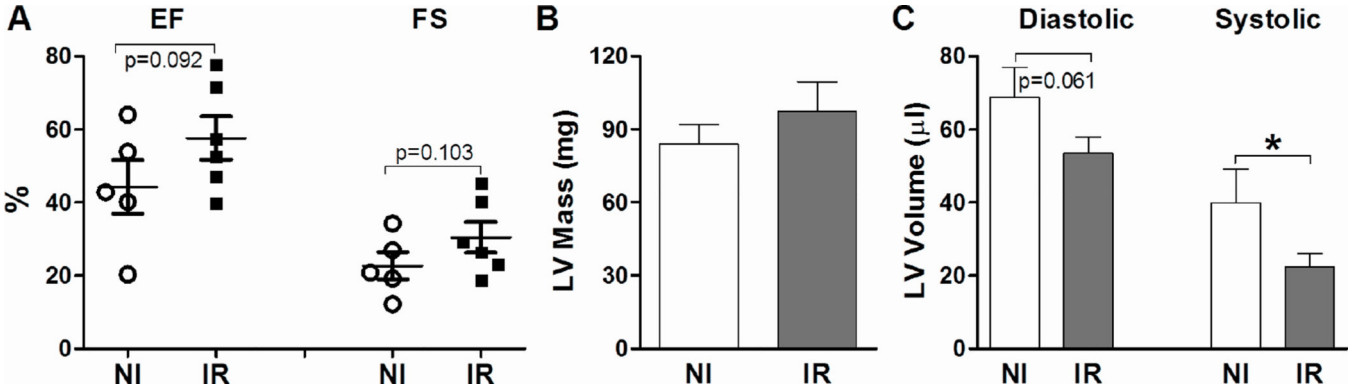

Fig. 7.

Assessment of cardiac function by echocardiography. Average results from echocardiography of IR mice at 18 mo post-TBI and their age-matched NI controls are shown in A for ejection fraction (EF) and fractional shortening (FS), B for left ventricular (LV) mass, and LV volumes in C. End systolic volume was significantly reduced and there was a trend suggesting reduced end diastolic volume and increased EF. Error bars are standard error of mean.

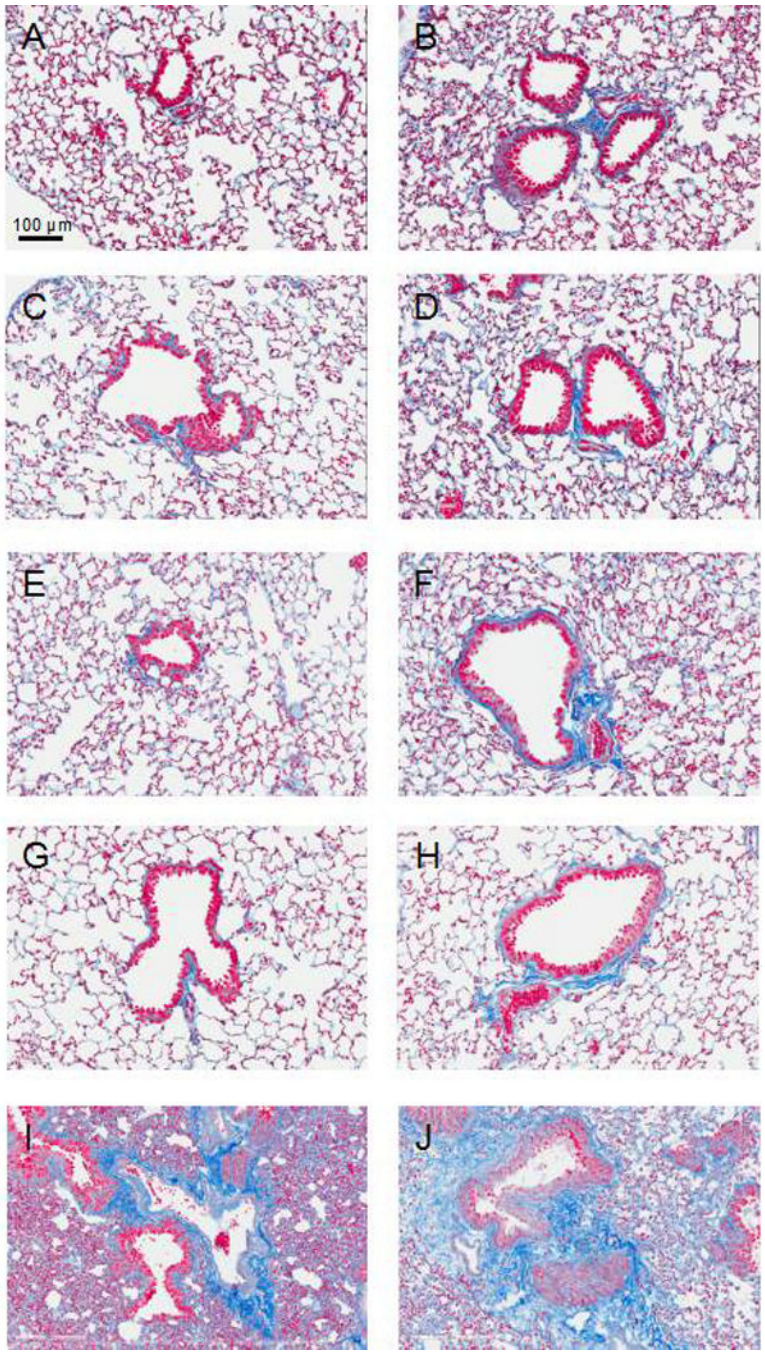

Fig. 8.

High magnification images (20×) of irradiated (right) and age-matched non-irradiated control (left) lungs slides stained with Masson's Trichrome. Slides shown include lung from mice at 1.4 (A and B), 5.8 (C and D), 6.4 (E and F), 7 (G and H) and 19 (I and J) months post-TBI. Pathological fibrosis can be seen detected around bronchioles and vascular beds as early as 6.4 months post-TBI and there is pronounced peribronchial, perivascular, and interstitial fibrosis at 19 months post-TBI.

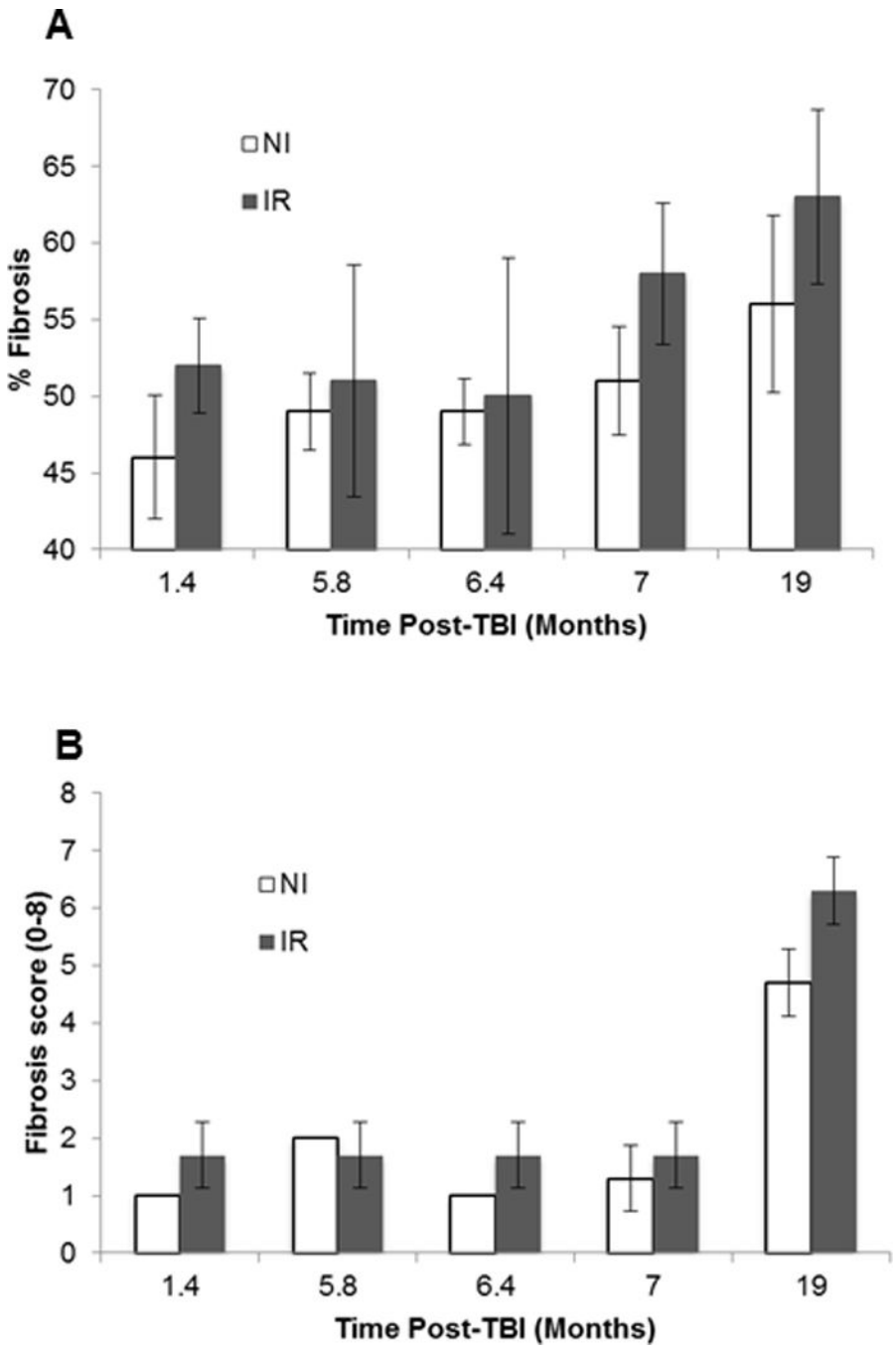

Fig. 9.

Quantitation of lung collagen by hand count and image analysis methods. A. Average pathology score from hand count. The score at 19 months post-TBI in the IR was significantly greater than the NI mice ($p=0.01$). For both IR and NI, the score at 19 mo was significantly greater than all other time points ($p<0.001$). B. Whole slide analysis of lung slides using Aperio software. With the computer-assisted image analysis, there were significant differences between the IR 19 mo values when compared to 1.4, 5.8, and 6.4 months ($p<0.02$). There were no differences among any of the NI time points, nor between

IR and NI. For both A and B, N=3 for each data point and error bars represent standard deviation.

Table 1

Histological Scoring Scale

Abnormality	Score
Sclerosed glomeruli (20 glomeruli/slide)	
0–5% sclerosed	0
6–25% sclerosed	1
26–50% sclerosed	2
51–75% sclerosed	3
> 75% sclerosed	4
Hypertrophied glomeruli	
none	0
>1	1
Tubularized glomeruli	
none	0
>1	1
Interstitial fibrosis	
Normal collagen	0
Diffuse, minimal	1
Diffuse, mininal with focal	2
Diffuse, significant	3
Protein Casts (# per slide)	
0–30	0
31–60	1
>60	2

Table 2

Histological scores for kidneys.

	1 Yr NI	1 Yr IR	2 Yr NI	2 Yr IR
Sclerosed glomeruli	0	1.75	0	3
Hypertrophied glomeruli	0	0	0	1
Tubularized glomeruli	0	0	0	0.75
Interstitial fibrosis	0	1.5	1.25	3
Protein casts	0.2	0.25	0.75	2
TOTAL Score	0.2	3.5	2	9.75

Table 3

Descriptive statistics for glomerular diameters.

Column	Mean	Std Dev	Std. Error	Range	Max	Min	Median	0.25	0.75
1Yr NI	80	15.1	1.51	68	120	51	78	70	87
1Yr IR	79	12.9	1.44	61	114	53	78	70	87
2Yr NI	86	13.1	1.31	62	123	60	82	77	95
2Yr IR	104	21.8	2.44	98	173	75	103	88	115